Geochemistry Geophysics Geosystems G3

Article
Volume 12, Number 4
5 April 2011
Q04D09, doi:10.1029/2010GC003417
ISSN: 1525-2027

Published by AGU and the Geochemical Society

Growth of borehole breakouts with time after drilling: Implications for state of stress, NanTroSEIZE transect, SW Japan

J. Casey Moore
Earth and Planetary Sciences Department, University of California, Santa Cruz, California 95064, USA (cmoore@pmc.ucsc.edu)

Chandong Chang
Department of Geology, Chungnam National University, Daejeon 305-764, South Korea (cchang@cnu.ac.kr)

Lisa McNeill
National Oceanography Center, University of Southampton, Southampton SO14 3ZH, UK (lcmn@noc.soton.ac.uk)

Moe Kyaw Thu
Center for Deep Earth Exploration, Japan Agency for Marine-Earth Science and Technology, 3173-25 Showa-machi, Kanazawa-ku, Kanagawa, Yokohama 236-0001, Japan (moe@jamstec.go.jp)

Yasuhiro Yamada
Civil and Earth Resources Engineering Department, Kyoto University, Kyoto 615-8540, Japan (yamada@earth.umst.kyoto-u.ac.jp)

Gary Huftile
Queensland University of Technology, GPO Box 2434, Brisbane, Qld 4001, Australia (g.huftile@qut.edu.au)

[1] Resistivity at the bit tools typically provide images of wellbore breakouts only a few minutes after the hole is drilled. In certain cases images are taken tens of minutes to days after drilling of the borehole. The sonic caliper can also image borehole geometry. We present four examples comparing imaging a few minutes after drilling to imaging from about 30 min to 3 days after drilling. In all cases the borehole breakouts widen with time. The tendency to widen with time is most pronounced within a few hundred meters below the seafloor (mbsf), but may occur at depths greater than 600 mbsf. In one example the widening may be due to reduced borehole fluid pressure that would enhance borehole failure. In the three other cases, significant decreases in fluid pressure during temporal evolution of breakouts are unlikely. The latter examples may be explained by time-dependent failure of porous sediments that are in an overconsolidated state due to drilling of the borehole. This time-dependent failure could be a consequence of dilational deformation, decrease of pore fluid pressure, and maintenance of sediment strength until migrating pore fluids weaken shear surfaces and allow spallation into the borehole. Breakout orientations, and thus estimates of stress orientations, remain consistent during widening in all four cases. In vertical boreholes, breakouts wider than those initially estimated by resistivity imaging would result in higher estimates of horizontal stress magnitudes. Because the vertical overburden stress is fixed, higher estimated horizontal stresses would favor strike-slip or thrust faulting over normal faulting.

Components: 7300 words, 10 figures.

Keywords: breakouts; subduction; NanTroSEIZE; Japan; Nankai; stress.

Index Terms: 8104 Tectonophysics: Continental margins: convergent; 8164 Tectonophysics: Stresses: crust and lithosphere.

Received 25 October 2010; **Revised** 8 February 2011; **Accepted** 14 February 2011; **Published** 5 April 2011.

Moore, J. C., C. Chang, L. McNeill, M. K. Thu, Y. Yamada, and G. Huftile (2011), Growth of borehole breakouts with time after drilling: Implications for state of stress, NanTroSEIZE transect, SW Japan, *Geochem. Geophys. Geosyst.*, *12*, Q04D09, doi:10.1029/2010GC003417.

Theme: Mechanics, Deformation, and Hydrologic Processes at Subduction Complexes, With Emphasis on the Nankai Trough Seismogenic Zone Experiment (NanTroSEIZE) Drilling Transect
Guest Editors: D. Saffer, P. Henry, and H. Tobin

1. Introduction

[2] Logging while drilling (LWD) resistivity at the bit (RAB) imaging has provided major advances for geodynamic, structural, and lithologic interpretation of Integrated Ocean Drilling Project (IODP) boreholes. The most dramatic results have estimated present-day stress orientations using both breakouts and structural data interpreted from the RAB images [*McNeill et al.*, 2004; *Goldberg and Janik*, 2006; *Weinberger and Brown*, 2006; *Ienaga et al.*, 2006; *Moore et al.*, 2009b; Y. Yamada et al., Structural styles across the Nankai Accretionary Prism revealed from LWD borehole images and its correlation to seismic profile: Results from IODP Expedition 314, submitted to *Geochemical Geophysics Geosystems*, 2010]. Stress magnitude has also been estimated from borehole breakouts [*Chang et al.*, 2010].

[3] The development of breakouts has been explained using a number of different mechanisms, which include brittle failures in shear [*Zoback et al.*, 1985], extensile fractures [*Zheng et al.*, 1989], or mixed mode fractures [*Zheng et al.*, 1989; *Cuss et al.*, 2003]. Experimental and numerical studies also indicate that breakouts develop progressively in depth with time; however, the width does not increase in time for constant stress conditions [*Zoback et al.*, 1985; *Hamison and Herrick*, 1989; *Cuss et al.*, 2003]. Rocks used in the experimental studies on borehole breakouts discussed above were either crystalline rocks or porous clastic rocks with some cementation.

[4] Here we report on porous, weak muddy sediments that appear to exhibit significant time-dependent growth of their borehole breakout geometry, especially their width. Such changes can introduce errors into inferences of stress orientations and stress magnitudes and need to be understood to evaluate borehole geomechanics and tectonics. In IODP boreholes in sediments, RAB images are our primary tool to study borehole breakouts. RAB images are normally collected within a few minutes of cutting of the borehole but may be delayed tens of minutes to days due to routine or exceptional borehole operations. We have examined a series of logging while drilling resistivity and ultrasonic caliper images, collected from a few minutes to days after cutting of the borehole. These images span the Nankai Trough Seismogenic Zone Experiment (NanTroSEIZE) transect of the subduction zone of SW, Japan (Figure 1), and represent the most complete set of IODP resistivity images across a continental margin, active or passive.

2. Geologic Setting of the Nankai Trough Subduction Zone Transect Across the Kumano Forearc

[5] The subduction of the Philippine Sea plate beneath southwest Japan forms the Nankai Trough and the associated accretionary prism. In the Kumano region estimates of the rate of subduction range from 4 to 6.5 cm/yr along azimuths of 300° to 315° [*Seno et al.*, 1993; *Miyazaki and Heki*, 2001; *Zang et al.*, 2002]. Along the NanTroSEIZE transect, the subduction direction is rotated about 15° to 30° counterclockwise from the dip azimuth of the margin, so there is a component of obliquity (Figure 1). The sedimentary sequence of the continental margin originated both from the deposits on the oceanic plate, that were structurally emplaced to form the accretionary prism, and sediments accumulated on the slope and in the forearc basin on top of the accretionary prism [*Kinoshita et al.*, 2009;

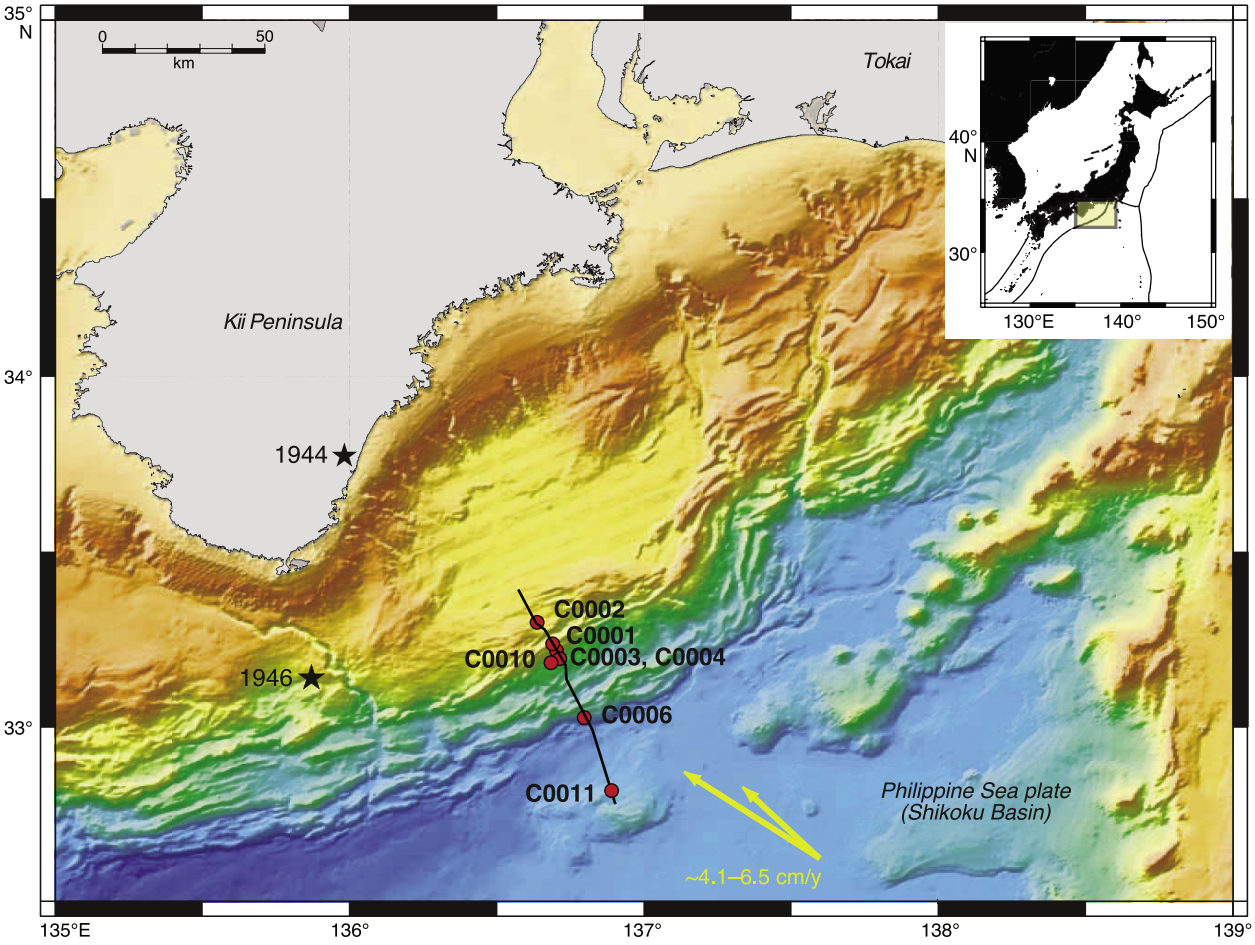

Figure 1. Location of IODP sites across NanTroSEIZE transect. Stars with dates indicate location and timing of great earthquake epicenters [*Ando*, 1975]. Yellow arrows show convergence directions between the Philippine Sea Plate and Japan [*Seno et al.*, 1993; *Miyazaki and Heki*, 2001; *Zang et al.*, 2002].

Saito et al., 2010]. Large-scale thrust faults dominate the structure of the margin [*Moore et al.*, 2007, 2009a]. Large apparently active megasplay (out-of-sequence thrust) faults emerge along the inner trench slope [*Moore et al.*, 2007] and may have slipped during the M 8.1 earthquake that occurred 1944 earthquake [*Baba and Cummins*, 2005]. Small-scale normal faults are common in the forearc basin [*Gulick et al.*, 2010]. Analysis of the cores from all sites studied here (Figure 1), reveal small-scale faults of normal, thrust, and strike-slip displacement [*Kinoshita et al.*, 2009].

[6] The borehole images analyzed here extend to more than 600 mbsf and are mostly in mud-mudstone, with local sand layers probably of turbidite origin [*Kinoshita et al.*, 2009; *Saffer et al.*, 2010; *Saito et al.*, 2010]. Both accreted and slope/forearc basin deposits are included in the images analyzed here. At the depths of the breakouts we studied, shipboard measurements of core sample's porosities range from greater than 60% to slightly less than 40% [*Kinoshita et al.*, 2009; *Saito et al.*, 2010].

3. Logging While Drilling Technology and Data Presentation

[7] The following discussion of logging tool specifications is taken from [*Bonner et al.*, 1994, 1996], plus personal communications from Schlumberger engineers during Expeditions 314 and 319. The resistivity at the bit tool records five different resistivity measurements, three of which are azimuthal (Figure 2). The azimuthal resistivity is recorded 56 times during each rotation of the bit or about once every 6.4 degrees of rotation. The azimuthal resistivity measurements are taken at shallow, medium and deep levels of investigation or approximately 2.5, 7.6, and 12.7 cm from the external surface of the tool [*Bonner et al.*, 1996]. In general it is most effective to use the shallow level of

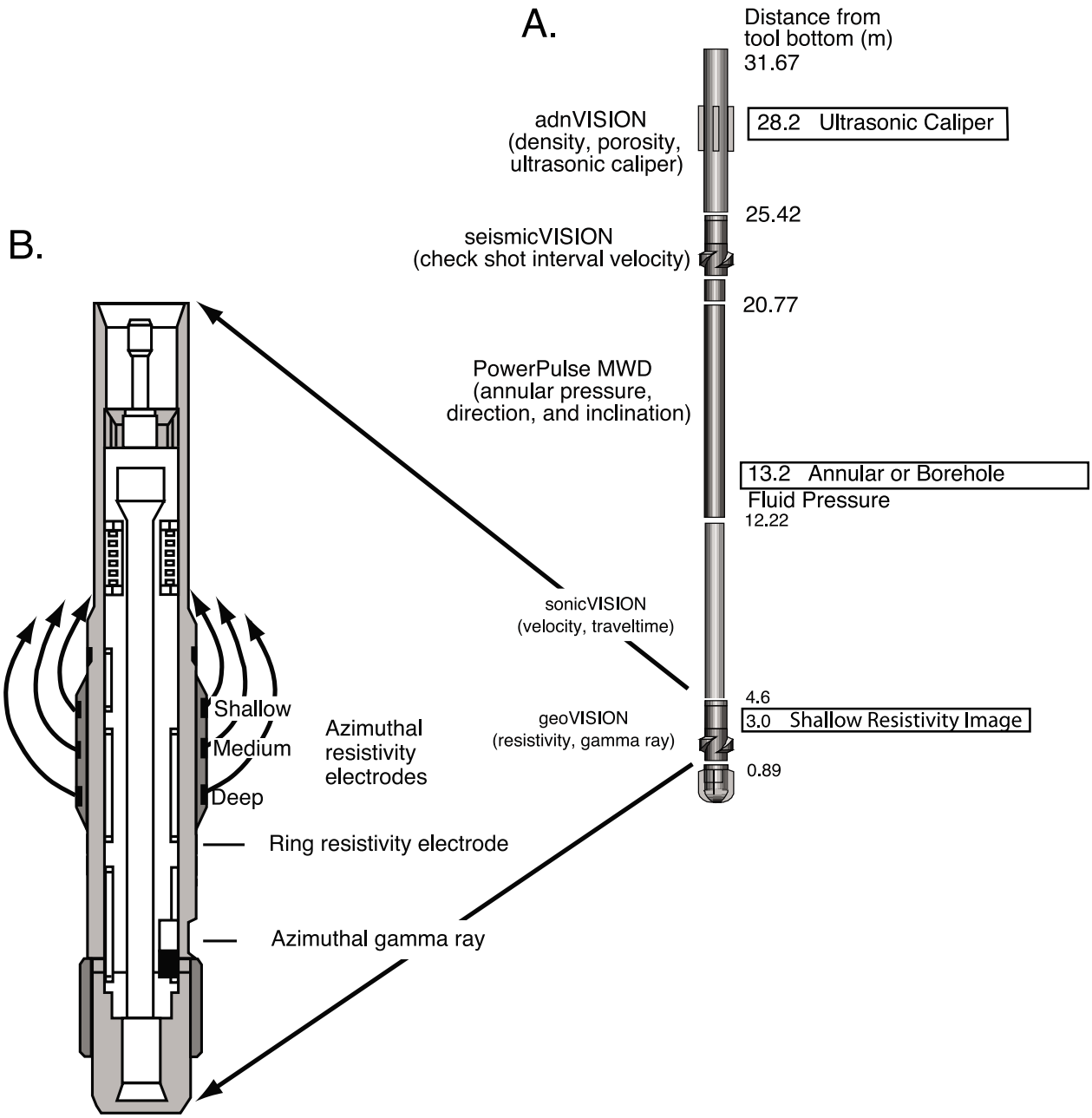

Figure 2. Schematic LWD logging tool string. (a) LWD tool string run at Sites C0001–C0003, noting distance above bit of measurements mentioned in text [*Expedition 314 Scientists*, 2009; *Expedition 319 Scientists*, 2010]. Sites C0004 and C0006 utilized a similar string, however without the adnVISION tool. Sites C0010 and C0011 used a tool string similar to Sites C0004 and C0006 (without adnVISION, seismicVISION, annular pressure, nor sonicVision), with a 12.25 in. bit and proportionally larger diameter resistivity tools [*Expedition 319 Scientists*, 2010]. (b) Detail of geoVISION tool measuring resistivity at the bit (RAB). Curved arrows indicate approximate imaging paths of shallow, medium and deep azimuthal resistivity measurements.

investigation when imaging the borehole for structural features and borehole failure. The horizontal resolution of the RAB images at shallow depth of investigation is about 2 cm for a 21.5 cm (8.5 inch) hole (drilled during Exp. 314) and about 2.5 cm for a 31.1 cm (12.25 inch) hole (drilled during Exp. 319) (Schlumberger, Pers. Com. 9/30/07). The vertical resolution is about 5–7.5 cm for either hole size.

[8] Although this paper focuses on the resistivity images, much of the ancillary data used to explain the images is from other logging tools (Figure 2).

Other tools in the drill string provide information on natural radioactivity (gamma ray), density, and locally hole size from a sonic caliper; these data were available as images with azimuthal sampling of 56 per revolution for gamma ray, and 16 per revolution for density and sonic caliper. The sonic caliper provided useful images whereas the gamma ray and density images were not sufficiently variable for image interpretation. The LWD tool assembly used during Exp 314 and 319 also recorded information about annular pressure while drilling, rate of penetration, and rate of rotation as part of measurement while drilling (MWD).

[9] The RAB image is recorded about 3 m above the bit. At a 30 m/h penetration rate, the image is recorded 6 min after the hole is cut. We have used the shallow level of investigation of the RAB images to best resolve the borehole wall for structural features and borehole failure. Images can be analyzed with "static" normalization (uniform gain throughout the borehole), or with dynamic normalization. In the latter, to better highlight small-scale features, gain is adjusted in a stepwise fashion according to the range of data in small depth intervals of the borehole. For consistency we show static normalization in most figures.

[10] The geometry of borehole failure or breakouts is widely used to infer present-day stress orientations both in industry and scientific boreholes [*Zoback*, 2007], and has been an important tool for understanding the state of stress in the Nankai trough [*McNeill et al.*, 2004; *Ienaga et al.*, 2006; *Tobin and Kinoshita*, 2009; *Lin et al.*, 2010]. In the shallow vertical wells that IODP commonly drills the vertical stress is typically a principal stress; moreover, breakouts and/or drilling-induced tensional fractures can be used to estimate stress orientations and magnitudes in a plane perpendicular to the borehole [*Moos and Zoback*, 1990; *Zoback*, 2007; *Chang et al.*, 2010].

[11] In a RAB image, breakouts are recognized as zones of decreased resistivity on opposite sides of the borehole. The decreased resistivity is interpreted as an enlarged area between the resistivity tool and the borehole wall where there is a greater volume of more conductive (less resistive) drilling fluid [*Goldberg and Janik*, 2006]. Because the minimum depth of investigation of the RAB tool is about 2 cm and breakouts narrow away from the borehole wall, the RAB image may show a smaller angular image of the breakout than its limits at the borehole wall. However, because of the possibility of focusing of the current into the more conductive breakout, this geometric effect is difficult to evaluate.

4. Examples of Temporal Evolution of Borehole Breakouts

[12] At a number of the NanTroSEIZE sites, borehole breakouts show evidence of growth through time. In each example below, we outline the breakout geometries observed by RAB and ultrasonic imaging, and document their temporal sequences. In section 4.1.2, we recount what is known about the drilling and fluid pressure conditions and any changes that could have altered the geometry of the breakouts. Following these examples we present a model of time-dependent failure that may explain the growth of breakouts and explore some of the implications for estimation of stress orientations and magnitudes.

4.1. Breakout Evolution During Addition of Pipe Sections

4.1.1. Breakout Geometry

[13] The most straightforward example of breakout growth with time is documented by the correlation of their widening with intervals of pipe addition to the drill string. At Site C0002 a particularly good example occurs from 397 to 480 mbsf encompassing three intervals where drilling stopped to add a 38 m stand of pipe (Figure 3a). The RAB image is normally collected about 6 min after cutting the borehole during drilling at a rate of 30 m/h. However, when pipe is added, drilling stops and the drill string is pulled off the bottom of the hole; in this case, the section between the bit and the RAB tool does not get imaged for 30 to 45 min after the hole is cut in these approximately 3 m intervals. Note that observed breakouts are narrow or absent *outside* of the areas where drilling stopped and imaging was delayed (Figure 3a). Similarly, at Site C0001, between 100 and 300 mbsf, the breakouts are wider and more uniformly developed in the intervals where the time after bit (TAB) increases from 6 min to 30 to 45 min following pipe stand addition (Figure 3b). At Site C0001 the correlation between wider breakouts and longer TAB is less pronounced from 200 to 300 mbsf than in the interval from 100 to 200 mbsf (Figure 3b).

[14] Correlations similar to those above, between TAB and breakout development during intervals of pipe addition, exist at all other LWD sites across the

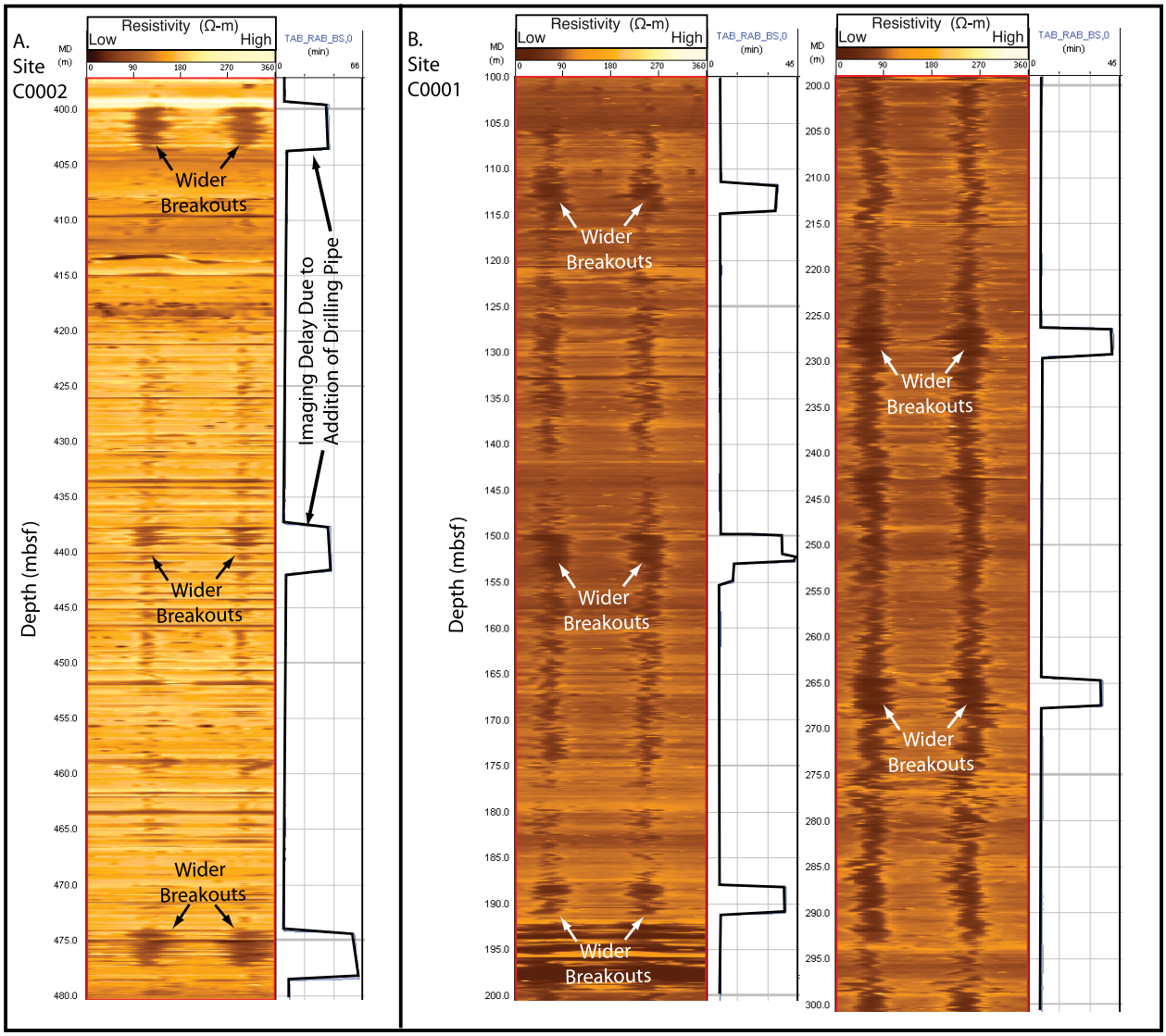

Figure 3. Resistivity images of breakouts verses time after bit (TAB) of imaging. (a) Site C0002. Note how breakouts widen at depths were TAB increases to about 40–45 min. (b) Site C0001. Breakouts also widen at depths with increased TAB, however, the effect is less pronounced than in C0002 and also less noticeable at greater depths (compare 200–300 mbsf versus 100–200 mbsf of Site C0001). Images are static and at a shallow depth of investigation.

NanTroSEIZE transect. However, not every interval of pipe addition and extended TAB is characterized by enhanced breakouts.

4.1.2. Drilling Conditions

[15] Addition of a 38 m "stand" of drill pipe involves pulling the bit off the bottom of the hole for at least 38 m while continuing to pump. The raising of the pipe over this interval is intended to clean the hole of cuttings. After returning the bit to the bottom of the hole, the pipe is raised 6 m off bottom with the pumps off and a new section is added. The fluid pressure, recorded while drilling, 13 m above the bit, was hydrostatic or slightly above in the examples noted (Figure 4). Because the pumping continues during raising of the pipe 38 m or more, it is likely fluid pressure conditions remain similar to those during drilling. However, when the pipe is raised 6 m from the bottom, with the pumps off, before adding a section, it is possible a suction or "swab" effect occurs below the bit, decreasing fluid pressure and perhaps enhancing borehole failure. Unfortunately, we have no means of evaluating the pressure at or below the bit at any time, because the pressure sensor is 13 m above the bit. A decrease in fluid

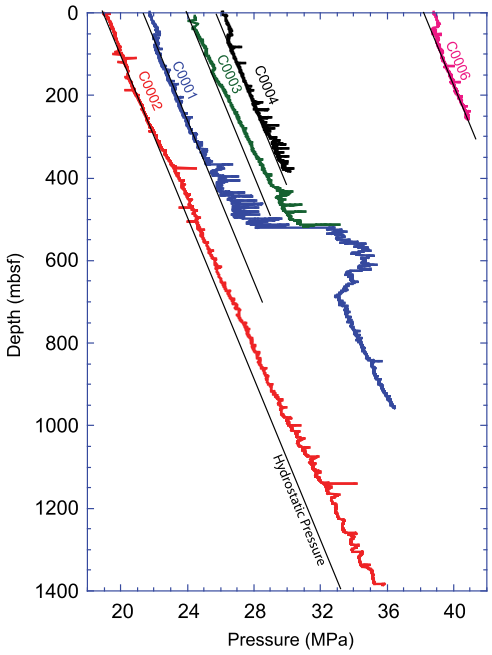

Figure 4. Borehole pressure measurements from measurement while drilling (MWD) tool (Figure 2). Borehole fluid pressures measure total pressure from sea level; hence, the progressive increase in pressure across the diagram represents increasing water depth. Holes generally show near-hydrostatic gradients from about 60 to 300 mbsf depth. Site C0002 shows pressure gradually increasing over hydrostatic with depth. C0001 and C0003 diverge from hydrostatic at shallower depths (200 to 400 mbsf) and were beset with significant drilling problems. Anomalously high pressures at depths of less than 60 mbsf at Sites C0001, C0004, and C0006 are probably due to unconsolidated sediments that create dense slurries in borehole annulus. Black lines represent fluid density of 1.04 g/cc, the probable upper limit for seawater density under borehole *P-T* conditions.

pressure would occur if the annulus between the bit and the borehole wall is clogged. When drilling resumes the lower 3 m of the borehole, the distance between the bit and the shallow resistivity sensor, is imaged. Finally there is a dynamic fluid pressure due to circulation, which would not be present when pumps are stopped. The variations in fluid pressure in the hydrostatic sections of pressure records suggest this dynamic effect is small, about 2% to 5% of total pressure at the depths we drilled (Figure 4).

4.2. Ultrasonic Caliper Images Verses RAB Images

4.2.1. Breakout Geometry

[16] Resistivity at the bit images are collected promptly, 3 m above the bit. In contrast, the ultrasonic caliper tool is located about 28 m above the bit (Figure 2), with a typical time lapse from hole cutting (TAB) of 55 to 95 min. Unfortunately the ultrasonic caliper operated only during the upper half of Site C0001, so we only have the one comparative imaging example for RAB and ultrasonic caliper.

[17] The ultrasonic caliper tool provides a direct measurement of borehole diameter at 16 intervals during each rotation of the bit [*Expedition 314 Scientists*, 2009]. These data are displayed as an image (Figure 5) and extracted as a direct measurement of borehole geometry (Figures 5 and 6). At Site C0001, an overlay of the limits of the breakouts from the resistivity image over the ultrasonic caliper image shows that the breakouts in the resistivity images are narrower and encompassed by the limits of the ultrasonic caliper breakout (Figure 5b). In this same interval, between 200 and 300 mbsf, the stacked ultrasonic caliper data indicates the breakouts have a maximum average depth of about 3–3.5 cm, dropping to an average depth of about one centimeter of hole enlargement between breakouts (Figure 6).

[18] The width of the breakouts, as seen both in the sonic caliper image (Figure 5) or inferred from the actual sonic caliper depth measurements (Figure 6), is greater than that inferred from the resistivity image. The average width of the breakouts measured by the shipboard scientific party in the 200 to 300 mbsf interval at C0001 is 40° [*Kinoshita et al.*, 2009]; this value includes the enlarged breakouts formed during the pipe stand additions, however. In contrast, the width of the breakouts measured from the average of the stacked ultrasonic caliper data is about 135° (Figure 6).

4.2.2. Drilling Conditions

[19] The expansion of breakouts documented by the ultrasonic caliper measurement apparently occurs under constant fluid pressure conditions. A pressure measurement in the annulus of the borehole (recorded ~10.2 m above the RAB imaging tool and ~13.2 m above the bit) indicates a hydrostatic gradient between 200 and 300 mbsf at Site C0001 (Figure 4). The consistent hydrostatic gradient from about 100 to about 350 mbsf at C0001 suggests that the RAB and ultrasonic caliper measurements were collected under similar pressure conditions in the 200 to 300 mbsf interval (Figure 4). Thus, the breakouts apparent in ultrasonic caliper measurements taken 50 to 100 min after drilling are not apparently enlarged by decreased fluid pressures in the borehole.

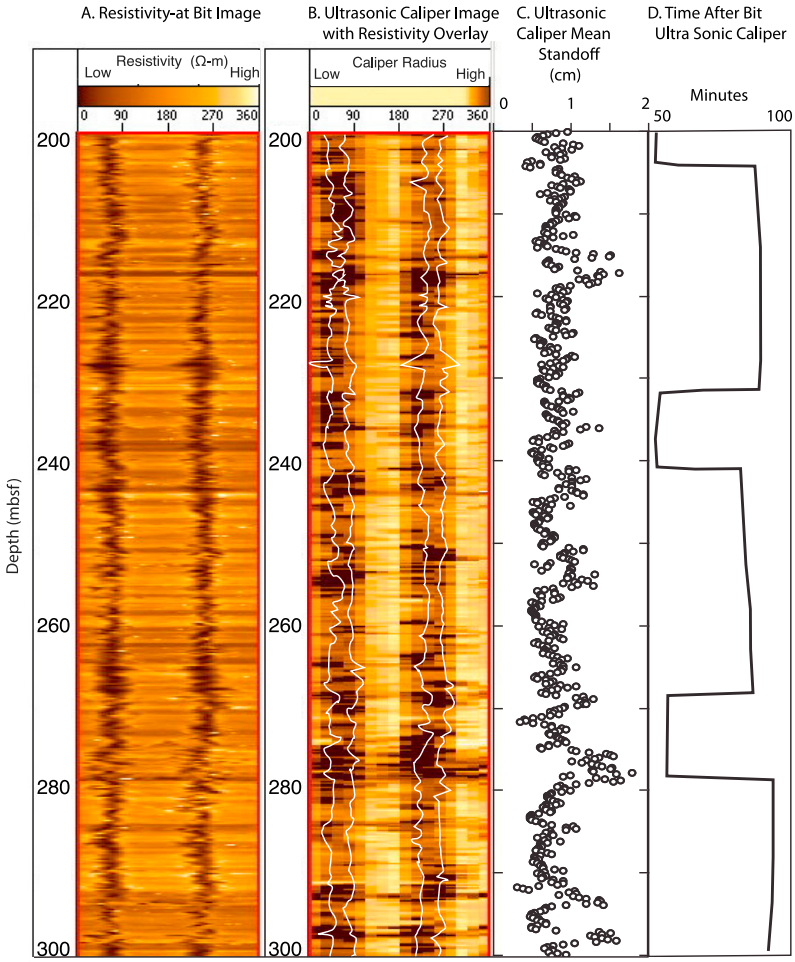

Figure 5. Comparison of resistivity and ultrasonic caliper images. (a) Resistivity at bit image overlies (b) ultrasonic caliper image. The ultrasonic caliper image is lower resolution than the resistivity image (16 verses 56 data points per revolution), but nevertheless the ultrasonic caliper images indicates wider breakout than the resistivity image. Darker colors of ultrasonic caliper image indicate larger borehole radius. Darker colors of resistivity image indicate higher conductivity, and inferentially larger borehole radius. Resistivity image is static and at a shallow depth of investigation. Caliper image is static. (c) Horizontal average of ultrasonic caliper data at each 15 cm sampling interval. Locally the holes are horizontally enlarged near 217 and 278 mbsf, probably due to washouts of silty-sandy intervals. (d) Time after bit (TAB) for ultrasonic caliper measurement. Note there is no correlation between TAB and hole enlargement (Figures 5b and 5c), suggesting progressive erosion by annular flow is not occurring.

[20] The ultrasonic caliper is located 28 m above the bit (Figure 2) and records the hole size from about 55 to about 90 min after the bit (TAB) (Figure 5d). The 55 min interval is time required to reach the ultrasonic caliper at a drilling rate of 30 m/h; the longer or about 90 min time interval is caused by the additional time required to add a section of pipe.

[21] Could the ultrasonic caliper diameter be larger than the resistivity measurement because of erosion of the hole by prolonged annular flow of 55 to about 90 min? A horizontally averaged mean standoff of the ultrasonic caliper tool (Figure 5c) shows no correlation to the longer TAB intervals (Figure 5d). Short sections of larger hole size in the horizontally averaged ultrasonic caliper (e.g., ~217 and ~278 mbsf, Figure 5c) appear to be stratigraphically controlled by local areas of lower resistivity, probably silty-sandy intervals. Moreover, the tendency of the hole enlargement in the ultrasonic caliper image to encompass that of the resistivity image suggests continuing breakout development as opposed to random hole erosion.

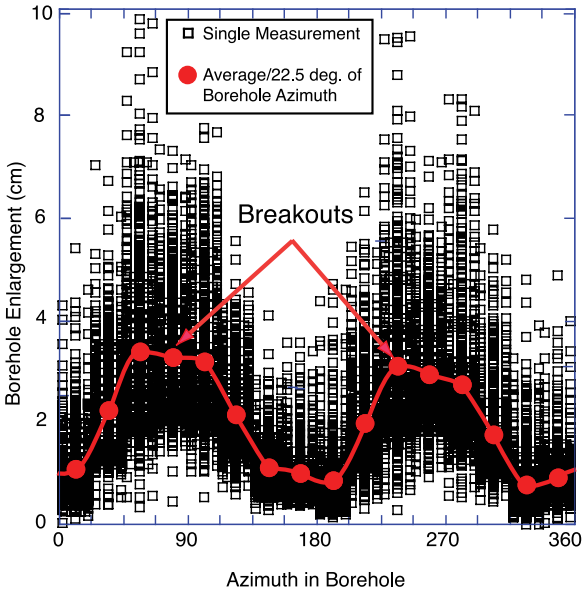

Figure 6. C0001 stacked sonic caliper data. Display shows 657 measurements from each 22.5° segment of borehole over 200–300 mbsf interval. The average of these values indicates a breakout width of 135°.

4.3. Imaging Open Hole 4–5 h After Drilling

4.3.1. Breakout Geometry

[22] Due to a technical problem halting drilling, a section of borehole between 602 and 630 mbsf at Site C0011 was not logged until almost 5 h after it was drilled (Figure 7) [*Expedition 322 Scientists*, 2010]. The breakouts are very clearly developed in this section. Portions of the borehole above and below this section were logged 6 to 7 min after the bit and show no breakouts (Figure 7). A section from 644 to 647 mbsf with a time after bit of up to 30 min shows weak development of breakouts. The section between 644 and 647 mbsf is at the depth of a pipe connection and suffered delays and failure comparable to those described in the Example 1, above.

4.3.2. Drilling Conditions

[23] Sediments at Site C0011, on the incoming oceanic crust, are cut by normal faults [*Saito et al.*, 2010] and therefore probably represent a low stress, extensional tectonic environment with the vertical stress equivalent to the maximum principal stress. In a vertical borehole in this environment, the difference between the maximum and minimum horizontal stresses, which drive breakouts, is suppressed. This state of stress probably explains why

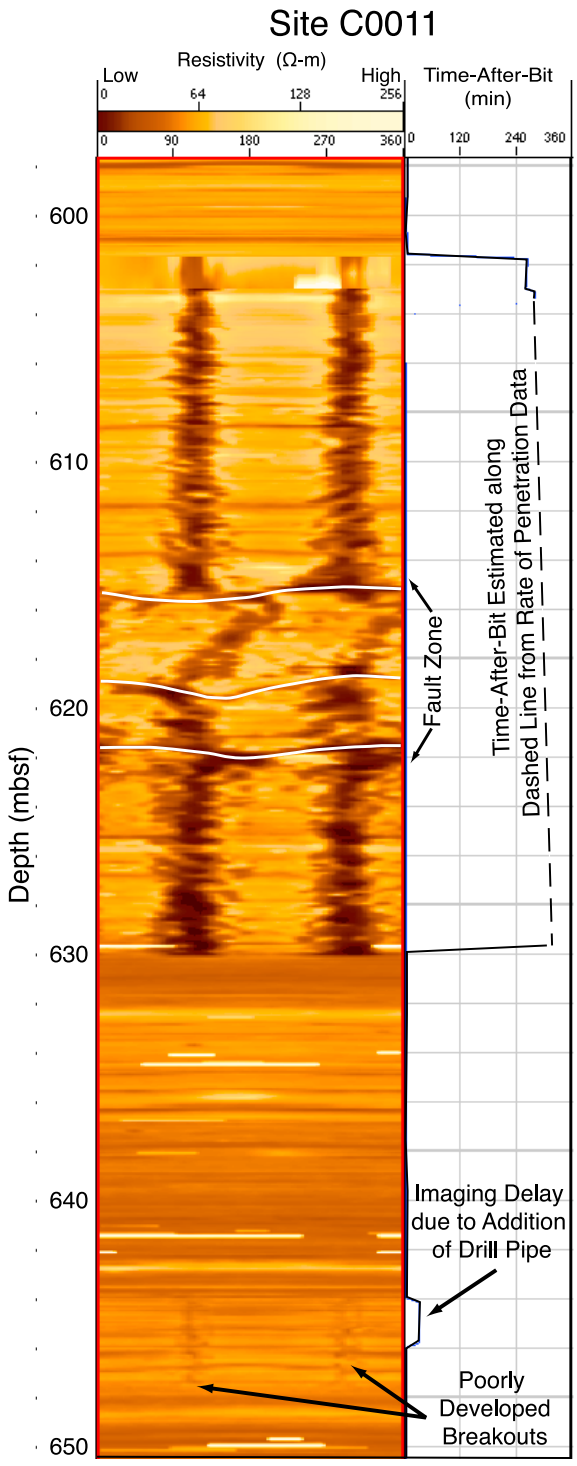

Figure 7. Site C0011: image of well-developed breakouts from 602 to 630 mbsf. These breakouts were imaged 4 to 5 h after cutting of the hole. Breakouts are not apparent elsewhere in the image, except for poorly developed examples in vicinity of ~45 min imaging delay due to addition of drill pipe at about 645 m. Breakout orientation is consistent, except in a fault zone. Images are static and at a shallow depth of investigation.

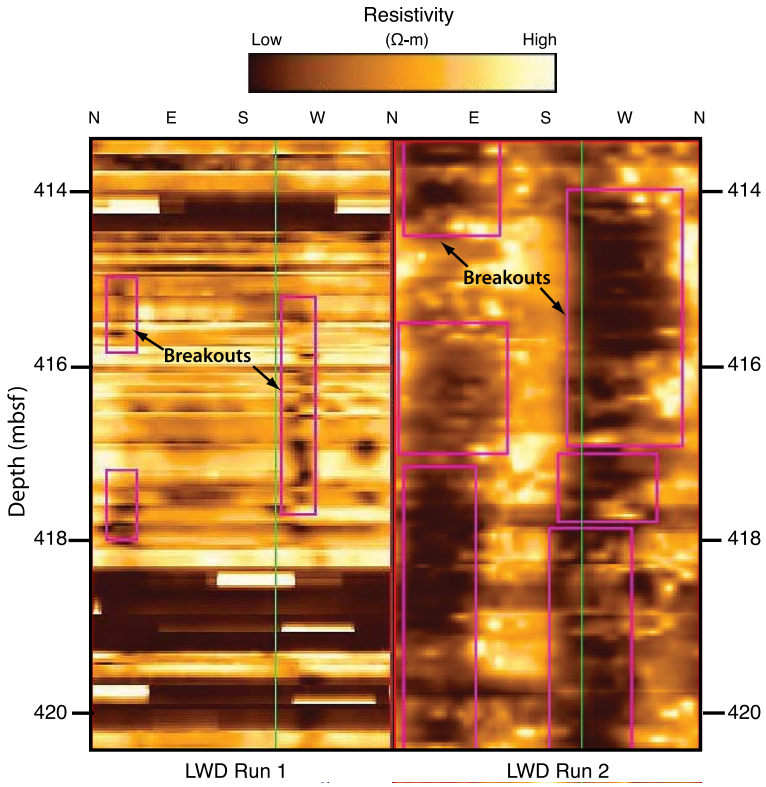

Figure 8. Site C0010: Note increasing size of breakouts in LWD run 2 versus run 1 of the same borehole. Run 2 was performed about 3 days after run 1. Green line indicates location of pad 1 azimuth. Run one is dynamically normalized and Run 2 is static. Both images are at a shallow level of investigation.

breakouts are poorly developed, except where there was a time lapse between drilling and imaging (Figure 7). Unfortunately no measurements of borehole fluid pressure were made during drilling of Site C0011. However, there is no reason to believe that the fluid pressure would drop sharply at C0011 during the 4–5 h time interval between drilling and collection of the images. Because the images between 602 and 630 mbsf were taken from an already drilled borehole, they were collected at a constant RPM with an absence of stick-slip [*Expedition 322 Scientists*, 2010], which improved image quality.

4.4. Borehole Images Collected 3 Days Apart

4.4.1. Breakout Geometry

[24] Site C0010 was abandoned on 9 August due to an imminent typhoon, and then reoccupied on 12 August and deepened. During the deepening, parts of the previously drilled hole were reimaged with the RAB tool, providing the longest time lapse of imaging runs over the NanTroSEIZE transect.

[25] The two images were collected 6–7 min and about 3 days after cutting the hole, respectively [*Saffer et al.*, 2010] (Figure 8). The image collected immediately after drilling shows very poorly developed narrow breakouts barely 25° wide. In contrast the image acquired 3 days later has breakouts that are about 125° wide.

4.4.2. Drilling Conditions

[26] No measurements were made of pressure in the borehole during drilling of Site C0010. However, measurements available at Site C0004, in a comparable setting 3.5 km along strike, show hydrostatic conditions (Figure 4). During abandonment, the hole was filled with seawater and there is no reason to expect any decrease in fluid pressure during this time.

5. Summary, Interpretations, and Implications

5.1. Summary of Observations

[27] Significant enlargement of breakouts occurs at all sites with LWD imaging during the 30 to 45 min pause to add pipe to the drill string. The growth of breakouts during pipe additions persists to greater

depths in boreholes associated with normal faulting (C0011 and C0002) than in those with seismically imaged thrust faults (C0001, C0004, C0006, and C0010). We cannot be certain that there is not a decrease in fluid pressure during the final raising of the pipe prior to the connection, which may explain breakout enlargement. The growth of breakouts in the ~50 to 90 min interval between RAB imaging and measurement by the sonic caliper apparently occurred during constant fluid pressure. Growth of breakouts is also apparent in relogged intervals from 4 to 5 h to 3 days after cutting the borehole. The operations during both of these hiatuses in drilling would be unlikely to cause decreases in fluid pressure. In all cases, the azimuths of narrow breakouts observed in images taken shortly after drilling are similar to the azimuths of the wider breakouts observed in images acquired later at the same location.

5.2. Options to Explain Breakout Growth

[28] The examples above clearly show that borehole breakouts may grow after their initial imaging a few minutes after the hole is cut. Breakouts form because the borehole concentrates the tectonic or far-field stresses and removes the radial support at the borehole wall [*Zoback*, 2007]. After the hole is drilled, the material at the borehole wall is subjected to the confining stress generated by the fluid pressure in the hole. In the case of the examples discussed above, the borehole fluid is seawater and the radial stress is less than was present before drilling.

[29] The most widely applied model for borehole failure involves estimation of stress magnitudes approximating the drilled material as an elastic solid with a Mohr-Coulomb failure criterion [*Zoback et al.*, 1985; *Moos and Zoback*, 1990; *Zoback*, 2007]. Irrespective of the failure model, removal of the lateral support of the borehole during drilling is the key factor causing failure. Over the time span of observed breakout growth, the tectonic stresses are unlikely to change, therefore some other explanation must account for breakout growth.

[30] Below we develop the concept of time-dependent failure in soft sediments, our favored model to explain the observations of breakout growth; however, there are other possible explanations. In section 4.1, we mentioned the possibility of a "swab effect," lowering the fluid pressure during the process of pipe addition to the drill string. This may only apply in this one case, so we have eliminated this as a general explanation of breakout growth with time. In section 4.2, we raised the issue of the erosion of the borehole during continued drilling. However, the evidence shows that vertical trends of hole enlargement are localized along the azimuth of the initial breakout direction, suggesting a continuing structural failure process. We cannot rule out the possibility that the flow of fluid through the annulus preferentially erodes incipiently failed breakouts that did not immediately spall into the borehole because of the cohesive nature of the sediment failure surface [*Moos et al.*, 2007]. Localized intervals of horizontal erosion do occur, however, these are best explained by sections of less cohesive sandy or silty beds. Finally, in section 4.4 the borehole was unoccupied during the three days when the breakout growth occurred, eliminating the possibility of erosion due to annular fluid flow. Overall we believe that the most likely process to explain the observed growth of breakouts is time-dependent failure of porous sediment.

5.3. Time-Dependent Borehole Failure With Constant Borehole Fluid Pressure

[31] The examples of enlargement of breakouts cited here involve boreholes under near hydrostatic pressure conditions, either as shown by direct measurements (Figure 4) or reasonably inferred from comparisons to other boreholes. Drilling the borehole changes the radial stress on the borehole wall from tectonic conditions to approximately hydrostatic, unloading the sediment at the borehole wall. The sediment in our images of breakouts is mudstone of low permeability (10^{-17} to 10^{-18}) m^2 [*Dugan and Daigle*, 2011; *Rowe et al.*, 2011; *Saffer et al.*, 2011]; therefore, these deposits undergo initial rapid deformation in a largely undrained state. We hypothesize that the expansion of the sediment by unloading and/or though dilational deformation, initially decreases fluid pressure near the borehole wall strengthening the sediment. We believe gradual weakening and breakout growth would occur as pore fluid migrates from the formation toward the borehole wall (shown diagrammatically in Figure 9).

[32] Dilational hardening or strengthening during undrained defomation of hard rocks is a well-known phenomena [*Paterson and Wong*, 2005]. Poorly consolidated sediments also show this behavior, as indicated by geotechnical studies of mudstones from IODP holes in the Gulf of Mexico [*Urgeles et al.*, 2007; *Dugan and Germaine*, 2009]. These experiments were conducted on silty-clay (stones) of about 40% porosity and are a good analog for the muddy sediments in the shallower parts of the NanTroSEIZE boreholes. Samples deformed in an overconsolidated state, under undrained conditions, show elastic-plastic

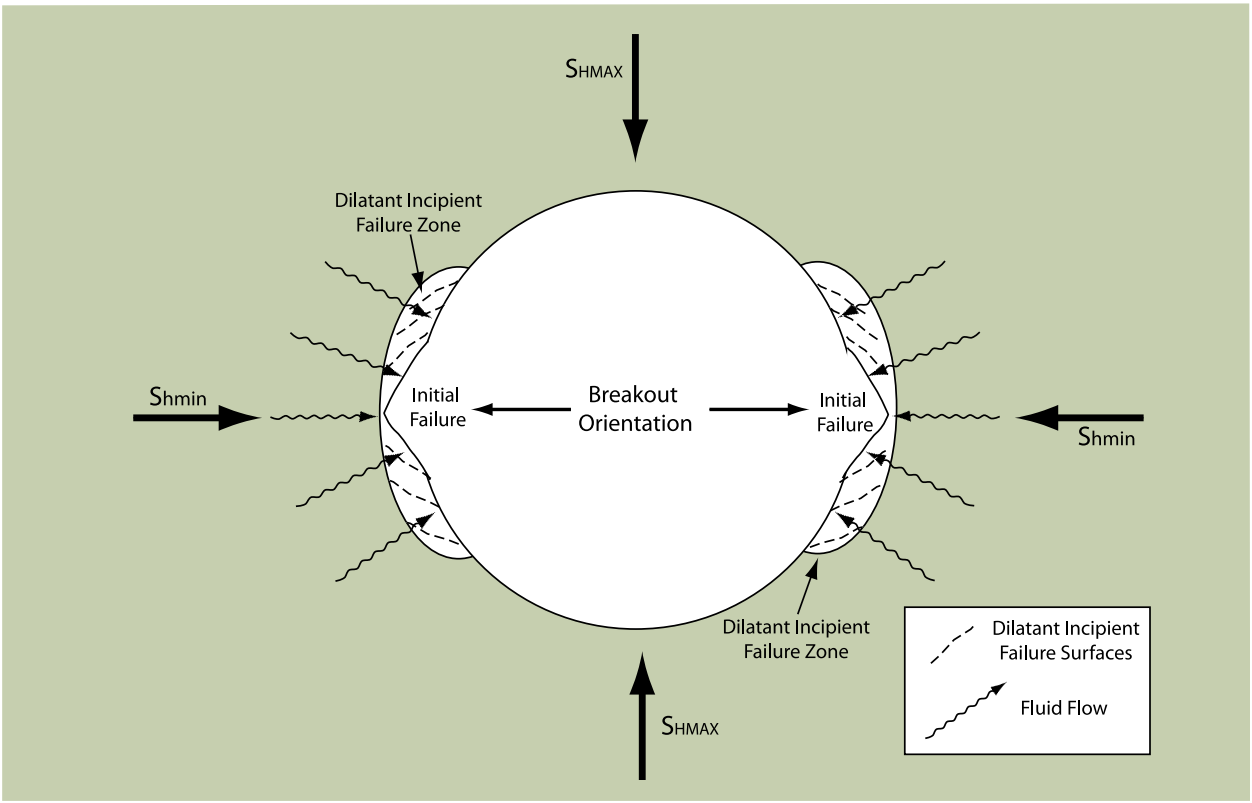

Figure 9. Schematic of time-dependent failure of a borehole. Initial failure occurs at area of highest stress concentration 90° from S_{HMAX}. Areas flanking initial failure undergo incipient undrained failure, but dilatant behavior of porous sediment prevents shear surfaces from weakening. Initial deformation occurs in an overconsolidated state due to release of confining pressure due to drilling of the borehole. Time-dependent fluid migration into incipient failure zones increases fluid pressure on failure surfaces ultimately resulting in their complete failure and spallation into the borehole. This diagram is modeled after general determination of hoop stress variations and therefore the failure propensity around the borehole using an elastic failure model [e.g., *Zoback*, 2007, Figure 6.3]. However, the model allows for failure geometry to be temporally modulated by changes in fluid pressure due to dilation and subsequent fluid migration into porous sediment.

deformation with no strain softening and a decline in pore pressure [e.g., *Moore et al.*, 2011, Figure 7b]. Apparently the decline in pore pressure is due to dilation that allows maintenance of sample strength. Because the borehole failures we observed were at an overconsolidated state, and initially undrained, dilational hardening probably occurred. Over time, the migration of fluid into the dilatant sediment would offset the lowered fluid pressure and allow failure. This process should allow the breakouts to progressively enlarge during this period of fluid pressure equalization (Figure 9).

5.4. Implications of Growth of Breakouts

[33] If breakouts grow by time-dependent failure under constant borehole fluid pressure, then their measurement in porous sediments within a few minutes after the bit underestimates their width. Also it is possible that the resistivity imaging systematically underestimates the width of the breakouts (see section 3). The width of a breakout is directly proportional to the magnitude of far field stresses [e.g., *Moos and Zoback*, 1990; *Zoback*, 2007; *Chang et al.*, 2010]. Underestimating the breakout width using the RAB images would therefore underestimate stress magnitude. However, we note that breakout azimuth is unchanged therefore measurements of stress orientation remain reliable.

[34] In order to quantitatively evaluate potential changes in stress magnitude and faulting conditions, we calculated horizontal stresses from the limiting measurements of breakout width from resistivity images and sonic caliper measurements from 200 to 300 mbsf at Site C0001, a vertical borehole (Figures 5 and 6). These stress polygons illustrate the range of possible horizontal stresses in the

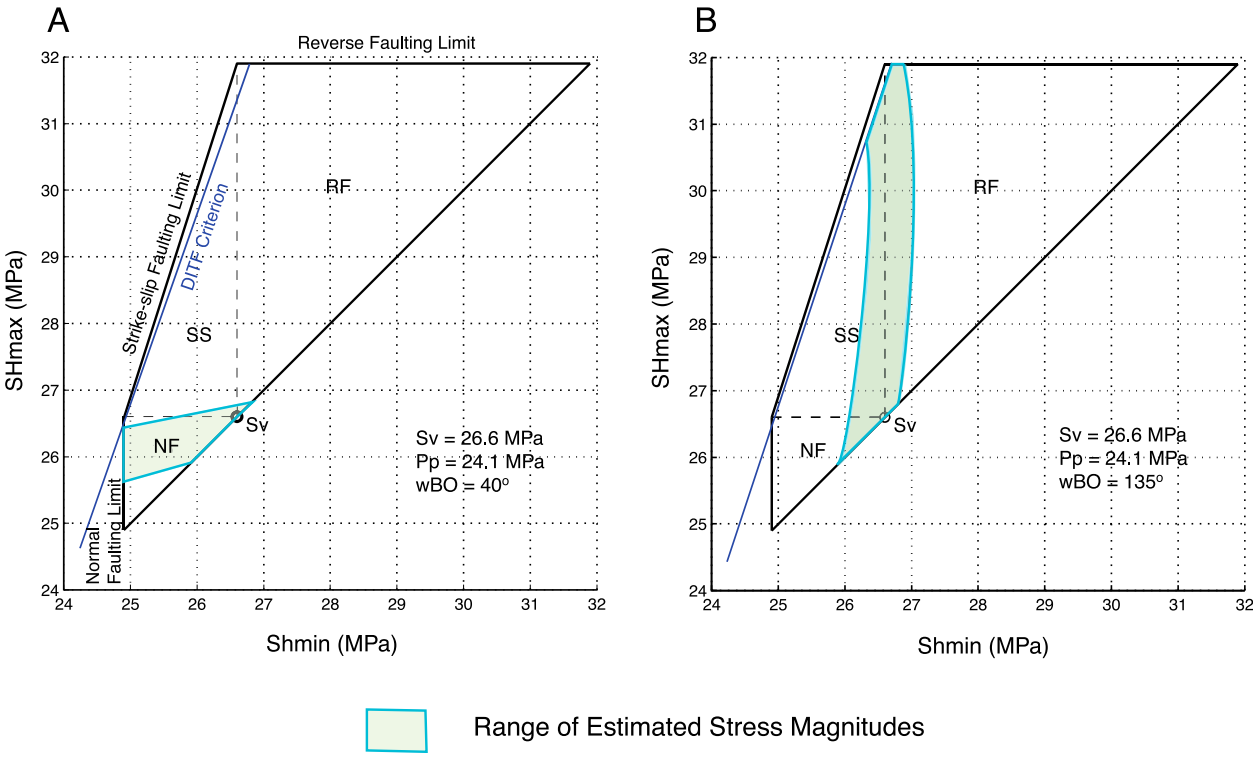

Figure 10. Estimated stress magnitudes for breakouts measured from Site C0001 at ~265 mbsf. (a) RAB image (40° breakout width or wBO) and (b) ultrasonic caliper (135° breakout width or wBO). Wider breakouts place the borehole in the realm of strike-slip and thrust faulting whereas narrower breakouts favor stress conditions associated with normal faulting. In each case stress magnitude range is variable because the range in estimates of unconfined compressive strength of the borehole wall rocks (2.6 to 3.9 MPa, inferred from velocity). Pore pressure (Pp) is assumed to be hydrostatic following *Chang et al.* [2010]. Estimates of stress magnitudes are plotted on a "stress polygon," which shows the limiting stress conditions for various types of faulting. For complete explanation of the methods applied to estimate the stresses see the study by *Chang et al.* [2010].

context of ratios of horizontal stresses that would produce normal, strike-slip, and reverse faulting (Figure 10). *Chang et al.* [2010] provide an overview of this approach and applies it to the drilling transect studied here. The breakout widths used to estimate the stresses represent the end-members from narrow to broad at one locality. The effect on stresses is profound, driving the section of borehole from a field of normal faulting to one lying on the boundary between strike-slip and reverse faulting. The tendency to move the stresses toward strike-slip or thrust faulting is due to the constant overburden, or vertical stress (Sv), and in the increase in maximum (S_{Hmax}) and minimum (S_{hmin}) horizontal stresses.

6. Conclusions

[35] With the more common usage of RAB imaging, breakouts have been discovered in many IODP holes. These images are recorded about 6 min after the hole is drilled at typical rates of penetration of 30 m/h. Off SW Japan we show that, at depths to 630 mbsf and porosities down to 40%, borehole breakouts in mudstones grow with time after drilling. Typically, the widths more than double in time spans of hours to days. In most cases this appears to occur at constant borehole fluid pressure conditions. Drilling replaces the tectonic confining stresses of the sediments with hydrostatic borehole fluid pressure, subjecting them to a transient effective stress regime associated with pore fluid pressure reduction and dilation. We believe the widening of the breakouts is due to the time-dependent deformation of porous cohesive sediment through a dilatant failure process. Although the width of the breakouts increases, the azimuth remains constant. RAB imaging of breakouts in porous sediments is robust for determining stress orientations but may systematically underestimate stress magnitudes perpendicular to the borehole; widening of breakouts with time leads to higher estimates of stresses in the plane perpendicular to the borehole leading to states

of stress favoring strike-slip or thrust faulting over normal faulting.

Acknowledgments

[36] We thank the governments of Japan, United States, and their partners in providing support for the NantroSEIZE drilling program during IODP. Moore thanks the U.S. Science Support Program for funding to participate in Expeditions 314 and 319 and for postcruise support to prepare this paper. We thank Geomechanics International for access to their Imager software for interpretation of resistivity images. We thank the scientific party of Expedition 322 for permission to use logging data from 600 to 650 mbsf at Site C0011. We appreciate the thoughtful reviews provided by Dan Moos and Demian Saffer.

References

Ando, M. (1975), Source mechanisms and tectonic significance of historical earthquakes along the Nankai Trough, Japan, *Tectonophysics*, *27*, 119–140, doi:10.1016/0040-1951(75)90102-X.

Baba, T., and P. R. Cummins (2005), Contiguous rupture areas of the two Nankai Trough earthquake revealed by high-resolution tsunami waveform inversion, *Geophys. Res. Lett.*, *32*, L08305, doi:10.1029/2004GL022320.

Bonner, S., A. Bagersh, B. Clark, G. Dajee, M. Dennison, J. S. Hall, J. Jundt, J. Lovell, R. Rosthal, and D. Allen (1994), A new generation of electrode resistivity measurements for formation evaluation while drilling, paper presented at 35th Annual Logging Symposium, Soc. of Petrophysicists and Well Log Anal., Tulsa, Okla.

Bonner, S., M. Fredette, J. Lovell, B. Montaron, R. Rosthal, J. Tabanou, P. Wu, B. Clark, R. Mills, and R. Williams (1996), Resistivity while drilling–Images from the string, *Oilfield Rev.*, *8*, 4–19.

Chang, C. D., L. McNeill, J. C. Moore, W. Lin, M. Conin, and Y. Yamada (2010), In situ stress state in the Nankai accretionary wedge estimated from borehole wall failures, *Geochem. Geophys. Geosyst.*, *11*, Q0AD04, doi:10.1029/2010GC003261.

Cuss, R. J., E. H. Rutter, and R. F. Holloway (2003), Experimental observations of the mechanics of borehole failure in porous sandstone, *Int. J. Rock Mech. Min. Sci.*, *40*(5), 747–761, doi:10.1016/S1365-1609(03)00068-6.

Dugan, B., and H. Daigle (2011), Data report: Permeability, compressibility, stress state, and grain-size of shallow sediments from the Sites C0004, C0006, C0007, and C0008 of the Nankai accretionary complex, in *NanTroSEIZE Stage 1: Investigations of seismogenesis, Nankai Trough, Japan*, *Proc. Integr. Ocean Drill. Program*, *314/315/316*, in press.

Dugan, B., and J. Germaine (2009), Data report: Strength characteristics of sediments from IODP Expedition 308, Sites U1322 and U1324, in *Gulf of Mexico Hydrogeology*, *Proc. Integr. Ocean Drill. Program*, *308*, doi:10.2204/iodp.proc.308.210.2009.

Expedition 314 Scientists (2009), Expedition 314 methods, in *NanTroSEIZE Stage 1: Investigations of seismogenesis, Nankai Trough, Japan*, *Proc. Integr. Ocean Drill. Program*, *314/315/316*, doi:10.2204/iodp.proc.314315316.112.2009.

Expedition 319 Scientists (2010), Methods, in *NanTroSEIZE Stage 2: NanTroSEIZE Riser/Riserless Observatory*, *Proc. Integr. Ocean Drill. Program*, *319*, doi:10.2204/iodp.proc.319.102.2010.

Expedition 322 Scientists (2010), Site C0011, in *NanTroSEIZE Stage 2: Subduction Inputs*, *Proc. Integr. Ocean Drill. Program*, *322*, doi:10.2204/iodp.proc.322.103.2010.

Goldberg, D., and A. Janik (2006), Data report: Stress orientation in gas hydrate–bearing sediments near Hydrate Ridge: Evidence from borehole breakouts observed from logging-while-drilling resistivity images [online], *Proc. Ocean Drill. Program Sci. Results*, *204*, 14 pp. (Available at http://www-odp.tamu.edu/publications/204_SR/108/108.htm.)

Gulick, S. P., N. L. Bangs, G. Moore, J. Ashi, K. M. Martin, D. S. Sawyer, H. T. Tobin, S. Kuramoto, and A. Taira (2010), Rapid forearc basin uplift and megasplay fault development from 3D seismic images of Nankai Margin off Kii Peninsula, Japan, *Earth Planet. Sci. Lett.*, *300*, 55–62, doi:10.1016/j.epsl.2010.09.034.

Hamison, B. C., and C. G. Herrick (1989), Borehole breakouts and in situ stress, *ETCE'99 Proc. ASME Energy Sources Technol. Conf.*, 17–22.

Ienaga, M., L. C. McNeill, H. Mikada, S. Saito, D. Goldberg, and J. C. Moore (2006), Borehole image analysis of the Nankai Accretionary Wedge, ODP Leg 196: Structural and stress studies, *Tectonophysics*, *426*, 207–220, doi:10.1016/j.tecto.2006.02.018.

Kinoshita, M., H. Tobin, J. Ashi, G. Kimura, S. Lallemant, E. J. Screaton, D. Curewitz, H. Masago, K. T. Moe, and Expedition 314/315/316 Scientists (2009), *Proceedings of the Integrated Drilling Program Expeditions*, vol. 314/315/316, Integr. Ocean Drill. Program, Washington, D. C., doi:10.2204/iodp.proc.314315316.2009.

Lin, W., et al. (2010), Present-day principal horizontal stress orientations in the Kumano forearc basin of the southwest Japan subduction zone determined from IODP NanTroSEIZE drilling Site C0009, *Geophys. Res. Lett.*, *37*, L13303, doi:10.1029/2010GL043158.

McNeill, L. C., M. Ienaga, H. Tobin, S. Saito, D. Goldberg, J. C. Moore, and H. Mikada (2004), Deformation and in situ stress in the Nankai Accretionary Prism from resistivity-at-bit images, ODP Leg 196, *Geophys. Res. Lett.*, *31*, L02602, doi:10.1029/2003GL018799.

Miyazaki, S., and K. Heki (2001), Crustal velocity field of southwest Japan: Subduction and arc-arc collision, *J. Geophys. Res.*, *106*, 4305–4326, doi:10.1029/2000JB900312.

Moore, G. F., N. L. Bangs, A. Taira, S. Kuramoto, E. Pangborn, and H. T. Tobin (2007), Three-dimensional splay fault geometry and implications for tsunami generation, *Science*, *318*, 1128–1131, doi:10.1126/science.1147195.

Moore, G. F., et al. (2009a), Three-dimensional splay fault geometry and implications for tsunami generation, in *NanTroSEIZE Stage 1: Investigations of seismogenesis, Nankai Trough, Japan*, *Proc. Integr. Ocean Drill. Program*, *314/315/316*, doi:10.2204/iodp.proc.314315316.102.2009.

Moore, J. C., G. J. Iturrino, P. B. Flemings, and D. E. Sawyer (2009b), Data report: Stress orientations from borehole breakouts, IODP Expedition 308, Ursa area, Mississippi Fan, Gulf of Mexico, in *Gulf of Mexico Hydrogeology*, *Proc. Integr. Ocean Drill. Program*, *308*, doi:10.2204/iodp.proc.308.212.2009.

Moore, J. C., R. Urgeles, M. Conin, P. Flemings, and G. J. Iturrino (2011), Threshold of breakout formation: Stress orientations and the mechanics borehole failure, Mississippi Fan, Gulf of Mexico, *Geosphere*, in press.

Moos, D., and M. L. Zoback (1990), Utilization of observations of borehole failure to contrain the oreination and

magnitude of crustal stresses: Application to continental, Deep Sea Drilling Project, and Ocean Drilling Program boreholes, *J. Geophys. Res.*, *95*, 9305–9325, doi:10.1029/JB095iB06p09305.

Moos, D., S. Wilson, and C. E. Barton (2007), Impact of rock properties on the relationship between wellbore breakout width and depth, in *Rock Mechanics: Meeting Society's Challenges and Demands, Proceedings of the 1st Canada-US Rock Mechanics Symposium, Vancouver, Canada, 27–31 May 200*, edited by E. Eberhardt, D. Stead, and T. Morrison, pp. 1677–1683, Taylor and Francis, London.

Paterson, M. S., and T.-F. Wong (2005), *Experimental Rock Deformation–The Brittle Field*, 2nd ed., 347 pp., Springer, New York.

Rowe, K., E. Screaton, J. Gou, and M. Underwood (2011), Data report: Permeabilities of sediments from the Kumano Basin transect offshore of the Kii Peninsula, Japan, in *NanTroSEIZE Stage 1: Investigations of Seismogenesis, Nankai Trough, Japan*, *Proc. Integr. Ocean Drill. Program*, *314/315/316*, in press.

Saffer, D., L. McNeill, T. Byrne, E. Araki, S. Toczko, N. Eguchi, and K. Takahashi, and the Expedition 319 Scientists (2010), *NanTroSEIZE Stage 2: NanTroSEIZE Riser/Riserless Observatory*, *Proc. Integr. Ocean Drill. Program*, *319*, in press.

Saffer, D., J. Guo, M. Underwood, W. Likos, R. Skarbeck, I. Song, and M. Gildow (2011), Data report: Consolidation and Permeability of sediments from the Nankai continental slope, IODP Sites C0001, C0008, and C0004, in *NanTroSEIZE Stage 2: NanTroSEIZE Riser/Riserless Observatory*, *Proc. Integr. Ocean Drill. Program*, *319*, doi:10.2204/iodp.proc.319XXXX.

Saito, S., M. B. Underwood, and Y. Kubo, and the Expedition 322 Scientists (2010), *NanTroSEIZE Stage 2: Subduction Inputs*, *Proc. Integr. Ocean Drill. Program*, *322*.

Seno, T., S. Stein, and A. E. Gripp (1993), A model for the motion of the Philippine Sea plate consistent with NUVEL-1 and geological data, *J. Geophys. Res.*, *98*, 17,941–17,948, doi:10.1029/93JB00782.

Tobin, H., and M. Kinoshita (2009), NanTroSEIZE Stage 1 summary, in *NanTroSEIZE Stage 1: Investigations of seismogenesis, Nankai Trough, Japan*, *Proc. Integr. Ocean Drill. Program*, *314/315/316*, doi:10.2204/iodp.proc.314315316.101.2009. (Available at http://publications.iodp.org/proceedings/314_315_316/111/111_.htm.)

Urgeles, R., J. Locat, and B. Dugan (2007), Recursive failure of the Gulf of Mexico continental slope: Timing and causes, in *Submarine Mass Movements and Their Consequences*, edited by V. Lykousis et al., pp. 207–219, Springer, Dordrecht, Netherlands.

Weinberger, J. L., and K. M. Brown (2006), Fracture networks and hydrate distribution at Hydrate Ridge, Oregon, *Earth Planet. Sci. Lett.*, *245*, 123–136, doi:10.1016/j.epsl.2006.03.012.

Zang, S. X., Q. Y. Chen, J. Y. Ning, Z. K. Shen, and Y. G. Liu (2002), Motion of the Philippine Sea plate consistent with the NUVEL-1A model, *Geophys. J. Int.*, *150*, 809–819, doi:10.1046/j.1365-246X.2002.01744.x.

Zheng, Z., J. Kemeny, and N. Cook (1989), Analysis of Borehole Breakouts, *J. Geophys. Res.*, *94*, 7171–7182, doi:10.1029/JB094iB06p07171.

Zoback, M. D. (2007), *Reservoir Geomechanics*, 449 pp., Cambridge Univ. Press, Cambridge, U. K., doi:10.1017/CBO9780511586477.

Zoback, M. L., D. Moos, L. Mastin, and R. N. Anderson (1985), Well bore breakouts and in situ stress, *J. Geophys. Res.*, *90*, 5523–5530, doi:10.1029/JB090iB07p05523.